

Effects of spin-destruction and spin-exchange collisions on alkali-metal relaxation and magnetometric response

Feng Tang(汤丰), Jianjun Li(李建军), and Nan Zhao(赵楠)

Citation: Chin. Phys. B, 2026, 35 (**4**): 043401. DOI: 10.1088/1674-1056/ae37f7
http://cpb.iphy.ac.cn; http://iopscience.iop.org/cpb

What follows is a list of articles you may be interested in

Single electron capture in low- and intermediate-energy collisions of $Si^{3,4+}$ with He

Yingzhou Li(李英卓), Yadong Liu(刘亚东), Yueying Qi(祁月盈), Ling Liu(刘玲), Yizhi Qu(屈一至), and Jianguo Wang(王建国)
Chin. Phys. B, 2026, 35 (**1**): 013401. DOI: 10.1088/1674-1056/ae15f4

Experiment study of energy redistribution during collisions of the excited state $H_2(1, 7)$ with LiH

Kai Wang(王凯), Zhong Liu(刘中), Shuying Wang(王淑英), Chu Qin(秦楚), Zilei Yu(於子雷), and Xiaofang Zhao(赵小芳)
Chin. Phys. B, 2025, 34 (**11**): 113401. DOI: 10.1088/1674-1056/add502

Electron excitation processes in low energy collisions of hydrogen-helium atoms

Kun Wang(王堃), Chuan Dong(董川), Yi-Zhi Qu(屈一至), Ling Liu(刘玲), Yong Wu(吴勇),Xu-Hai Hong(洪许海), and Robert J. Buenker
Chin. Phys. B, 2022, 31 (**12**): 123401. DOI: 10.1088/1674-1056/aca14c

Atomic structure and collision dynamics with highly charged ions

Xinwen Ma(马新文), Shaofeng Zhang(张少锋), Weiqiang Wen(汶伟强), Zhongkui Huang(黄忠魁), Zhimin Hu(胡智民), Dalong Guo(郭大龙), Junwen Gao(高俊文), Bennaceur Najjari, Shenyue Xu(许慎跃), Shuncheng Yan(闫顺成), Ke Yao(姚科), Ruitian Zhang(张瑞田), Yong Gao(高永), and Xiaolong Zhu(朱小龙)
Chin. Phys. B, 2022, 31 (**9**): 093401. DOI: 10.1088/1674-1056/ac8736

The influence of collision energy on magnetically tuned ^{6}Li-^{6}Li Feshbach resonance

Rong Zhang(张蓉), Yong-Chang Han(韩永昌), Shu-Lin Cong(丛书林), and Maksim B Shundalau
Chin. Phys. B, 2022, 31 (**6**): 063402. DOI: 10.1088/1674-1056/ac4cc3

Effects of spin-destruction and spin-exchange collisions on alkali-metal relaxation and magnetometric response

Feng Tang(汤丰)[1,†], Jianjun Li(李建军)[2,†], and Nan Zhao(赵楠)[1,‡]

[1] *Beijing Computational Science Research Center, Beijing* 100193, *China*

[2] *State Key Laboratory of Photonics and Communications, School of Electronics, and Center for Quantum Information Technology, Peking University, Beijing* 100871, *China*

(Received 4 November 2025; revised manuscript received 23 December 2025; accepted manuscript online 14 January 2026)

Spin-exchange (SE) and spin-destruction (SD) collisions play a central role in determining the coherence properties of alkali-metal vapors and the performance of alkali-metal magnetometers in external magnetic fields. In this work, we investigate how these collisions influence spin relaxation dynamics and magnetometric response using a generalized Bloch equation that fully accounts for the coupled evolution of spin polarizations in different hyperfine manifolds. Our results show that in the low-field regime, both SE and SD collisions contribute to the suppression of transverse spin relaxation and the slowdown of spin precession, whereas longitudinal relaxation depends weakly on the SE rate and is predominantly governed by SD interactions. Building on the established relationship between spin relaxation rates and magnetometric response, we further analyze how SE and SD collisions affect the performance of two representative magnetometer architectures: the spin-exchange relaxation-free (SERF) magnetometer and the magnetic-resonance Mx-type magnetometer. The SERF magnetometer's response is found to be primarily determined by the SD rate, with only minor dependence on the nuclear spin quantum number. In contrast, the magnetic-resonance Mx-type magnetometer's sensitivity is significantly affected by both the magnetic field strength and the SE rate. While the resonance linewidth decreases with reduced magnetic field, the associated measurement accuracy deteriorates markedly. Consequently, reliable magnetic field reconstruction is only achievable in the high-field regime, where the Larmor frequency greatly exceeds the SE rate.

Keywords: spin-exchange collision, spin-destruction collision, magnetometric response

PACS: 34.50.–s, 34.80.Nz, 07.55.Ge

DOI: 10.1088/1674-1056/ae37f7 **CSTR:** 32038.14.CPB.ae37f7

1. Introduction

Atomic magnetometers based on alkali-metal vapors have become indispensable tools for detecting weak magnetic fields, finding wide applications in biomagnetic diagnostics,[1,2] geophysical surveying, and fundamental physics research.[3,4] Their exceptional sensitivity arises from the ability to maintain long-lived spin coherence in hot atomic ensembles. However, this coherence is strongly affected by binary collisions between atoms, in particular, spin-destruction (SD) and spin-exchange (SE) collisions.[5,6] These collisional processes govern the relaxation and polarization dynamics of the ensemble and hence play a central role in determining both the sensitivity and accuracy of alkali-metal magnetometers.[7,8]

Several theoretical approaches have been developed to model spin relaxation and polarization under the influence of SD and SE collisions. The density matrix formalism provides the most complete quantum-mechanical description,[5] and numerical simulations based on the density matrix have shown excellent agreement with experimental observations, particularly in high-density alkali-metal vapors.[9] However, the full numerical treatment is computationally demanding and often impractical for analytical exploration or broad parameter scans.

In the spin-exchange relaxation-free (SERF) regime, where the spin-exchange rate is much larger than the Larmor frequency, a more intuitive and widely adopted alternative is the Bloch equation model,[7,10] particularly in the spin-temperature approximation. This model assumes that rapid spin-exchange collisions maintain a spin-temperature distribution among the hyperfine sublevels, which allows the system to be described by a single collective spin vector. While effective in describing low-field dynamics under strong spin-exchange rates, it has limited validity in regimes with moderate to high magnetic fields.

To overcome these limitations, a generalized theoretical framework — referred to as the hyperfine Bloch equations (HBE) — has been introduced.[11–13] Derived from the density matrix under the assumption of low polarization, the HBE formalism enables the analytic treatment of spin expectation values while retaining the ability to explore arbitrary magnetic fields and a broad range of spin-exchange rates. It thus bridges the gap between full quantum simulations and simplified Bloch models, offering a powerful tool for investigating

[†]These authors contributed equally to this work.

[‡]Corresponding author. E-mail: nzhao@csrc.ac.cn

© 2026 Chinese Physical Society and IOP Publishing Ltd. All rights, including for text and data mining, AI training, and similar technologies, are reserved.

relaxation and polarization phenomena in hot atomic vapors.

The HBE framework has been successfully employed in several contexts, including the study of inter-species spin relaxation,[12] magnetic-field-induced relaxation suppression,[14] and the characterization of spin noise spectra in hot vapors.[15] However, a comprehensive understanding of how SD and SE collisions jointly influence both transverse and longitudinal spin relaxation, and how these effects propagate to measurable magnetometric responses, remains incomplete.

In this work, we use the HBE formalism to systematically investigate the role of SD and SE collisions in shaping spin relaxation dynamics under arbitrary field and collision conditions. Particular attention is paid to the differential behaviors of longitudinal and transverse relaxation rates, revealing distinct dependencies on the collisional parameters. We further explore how these relaxation mechanisms impact the response characteristics of two representative magnetometer configurations: the SERF magnetometer and the magnetic-resonance Mx-type magnetometer. By establishing quantitative relations between collision rates and key performance metrics — such as linewidth and measurement accuracy — we provide predictive insights into the parameter regimes where high sensitivity and accurate field reconstruction are achievable. Our results serve as a unified theoretical foundation for optimizing atomic magnetometry across diverse operational regimes.

2. The hyperfine Bloch equation

The density matrix equation

$$\begin{aligned}\frac{\mathrm{d}\rho}{\mathrm{d}t} =& \frac{A_{\mathrm{hf}}}{\mathrm{i}\hbar}[\boldsymbol{I}\cdot\boldsymbol{S},\rho]+\frac{g_s\mu_{\mathrm{B}}}{\mathrm{i}\hbar}[\boldsymbol{B}\cdot\boldsymbol{S},\rho]+\Gamma_{\mathrm{SD}}(\varphi-\rho)\\&+\Gamma_{\mathrm{SE}}[\varphi(1+4\langle\boldsymbol{S}\rangle\cdot\boldsymbol{S})-\rho]\\&+R_{\mathrm{op}}[\varphi(1+2\boldsymbol{s}\cdot\boldsymbol{S})-\rho]\end{aligned}\tag{1}$$

provides the most precise model to describe experimental results quantitatively, when high-pressure approximation is well satisfied.[5] The evolution of the density matrix ρ arises from several distinct physical processes. The first term accounts for the contribution of hyperfine interactions between the nuclear spin $\boldsymbol{I}$ and electronic spin $\boldsymbol{S}$, with hyperfine coupling constant A_{hf}. The second term represents the Zeeman interaction between the external magnetic field $\boldsymbol{B}$ and the electron spin, where the much weaker nuclear Zeeman interaction with $\boldsymbol{B}$ is ignored. The third term describes spin-destruction relaxation, typically caused by collisions with buffer gas or quenching gas atoms. The SD processes completely destroy the electronic spin polarization while the nuclear spin remains unaffected, as SD collisions drive the alkali-metal ensemble to a steady state $\varphi=(\mathrm{Tr}_S\rho)\otimes(I_S/2)$ at a rate Γ_{SD}. The fourth term originates from spin-exchange collisions between alkali-metal atoms, which redistribute spin populations among different hyperfine states. Finally, the last term captures the effect of optical pumping on the D1 line, which drives spin polarization through resonant absorption and spontaneous emission processes. In the high-pressure limit, the optical pumping effects on ρ are described by a spin-exchange process between photon spin $\boldsymbol{s}$ and electronic spin $\boldsymbol{S}$ occurring at a rate R_{op}.[6,16]

Under typical magnetometer operating conditions, the hyperfine coherence terms in the density matrix can be safely neglected.[9] This is because no microwave fields are applied to drive transitions between hyperfine levels, and all relevant collisional rates (including spin-exchange and spin-destruction processes) are much smaller than the hyperfine splitting of the alkali-metal ground state. In these cases, the evolution of the density matrix

$$\rho=\mathcal{P}_a\rho\mathcal{P}_a+\mathcal{P}_b\rho\mathcal{P}_b\equiv\rho_a+\rho_b\tag{2}$$

will give an effective description of the alkali-metal atoms, where $\mathcal{P}_{a,b}$ represents the projection operator onto the hyperfine subspaces $F=I+1/2\equiv a$ and $F=I-1/2\equiv b$.

In magnetometers, special focus is paid to the evolution of spin expectations, since the measured signals are directly proportional to their values along the probe beam. Instead of using a Bloch equation for the total polarization,[8,10] we focus on the evolution of angular components

$$\langle\boldsymbol{F}_a\rangle=\mathrm{Tr}(\boldsymbol{F}\rho_a),\quad\langle\boldsymbol{F}_b\rangle=\mathrm{Tr}(\boldsymbol{F}\rho_b),\tag{3}$$

since all SD and SE collisions cause couplings of a and b subspaces, as well as the optical pumping process. Here, $\boldsymbol{F}=\boldsymbol{I}+\boldsymbol{S}$ denotes the total angular momentum of ground-state alkali-metal atoms. In the following, we omit the expectation value brackets $\langle\cdot\rangle$ for brevity, and quantities such as $\boldsymbol{F}_a$ and $\boldsymbol{F}_b$ are to be understood as their corresponding expectation values unless otherwise stated.

The evolution of $\boldsymbol{F}_{a,b}$ can be readily derived in the low polarization regime,[11–13,17] where only linear SE interactions are retained,

$$\frac{\mathrm{d}}{\mathrm{d}t}\boldsymbol{F}_a=\boldsymbol{F}_a\times\gamma_a\boldsymbol{B}+M_{aa}\boldsymbol{F}_a+M_{ab}\boldsymbol{F}_b+R_{\mathrm{op}}G_a\boldsymbol{s},\tag{4}$$

$$\frac{\mathrm{d}}{\mathrm{d}t}\boldsymbol{F}_b=\boldsymbol{F}_b\times\gamma_b\boldsymbol{B}+M_{ba}\boldsymbol{F}_a+M_{bb}\boldsymbol{F}_b+R_{\mathrm{op}}G_b\boldsymbol{s}.\tag{5}$$

The gyromagnetic ratio γ_a of the a-hyperfine manifold is given by

$$\gamma_a=\frac{g_s\mu_{\mathrm{B}}}{(2I+1)\hbar},\tag{6}$$

where g_s is the electron g-factor and μ_{B} is the Bohr magneton. The corresponding gyromagnetic ratio of the b-hyperfine manifold is $\gamma_b=-\gamma_a$, since the coupling between the nuclear spin $\boldsymbol{I}$ and the external magnetic field $\boldsymbol{B}$ has been neglected in Eq. (1).

The coupling coefficients appearing in Eqs. (4) and (5) form the elements of the relaxation matrix $\boldsymbol{M}$, which describes the damping of spin polarization due to both spin-destruction and spin-exchange collisions. It is given by

$$\boldsymbol{M} = \Gamma_{\rm SDT}\,\boldsymbol{M}_{\rm SD} + \Gamma_{\rm SE}\,\boldsymbol{M}_{\rm SE} = \begin{pmatrix} M_{aa} & M_{ab} \\ M_{ba} & M_{bb} \end{pmatrix}, \tag{7}$$

where $\Gamma_{\rm SDT} = \Gamma_{\rm SD} + \Gamma_{\rm SE} + R_{\rm op}$ is the total damping rate including optical pumping. The SD contribution arises from the so-called S-damping process:

$$\boldsymbol{M}_{\rm SD} = -\frac{1}{(1+2I)^2}\begin{pmatrix} 2I^2+I+1 & -(1+I)(3+2I) \\ I(1-2I) & 2I^2+3I+2 \end{pmatrix}, \tag{8}$$

while the SE relaxation matrix is given by

$$\boldsymbol{M}_{\rm SE} = \frac{1}{3(1+2I)^2}\begin{pmatrix} (1+I)(3+2I) & -(1+I)(3+2I) \\ -I(2I-1) & I(2I-1) \end{pmatrix}. \tag{9}$$

The optical pumping process introduces a source term that generates spin polarization along the pump direction $\boldsymbol{s}$, with polarization transfer coefficients

$$G_a = \frac{(1+I)(3+2I)}{6(1+2I)}, \tag{10}$$

$$G_b = \frac{I(1-2I)}{6(1+2I)}. \tag{11}$$

Compared to the simplified Bloch equation with slowing-down factors,[8,10] the HBE provides a more complete and physically grounded framework by explicitly accounting for the couplings between the a and b hyperfine subspaces induced by SD and SE collisions. In the conventional Bloch model, it is commonly assumed that the $\boldsymbol{F}_a$ and $\boldsymbol{F}_b$ manifolds precess together at a common Larmor frequency, which is modified by the slowing-down factor to account for hyperfine mixing in the high-$\Gamma_{\rm SE}$ limit. In contrast, the HBE formalism does not rely on this approximation and instead treats the distinct evolution of the two subspaces directly. Furthermore, the HBE remains valid beyond the SERF regime, where the Larmor frequency $|\gamma_{a,b}\boldsymbol{B}|$ becomes comparable to or larger than SE rate $\Gamma_{\rm SE}$, enabling accurate modeling of spin dynamics across a broad parameter space.

In the following sections, alkali-metal atoms with nuclear spin $I = 3/2$, such as ^{87}Rb and ^{39}K, are used as examples. By substituting the relevant coefficients into Eqs. (4) and (5), we obtain the corresponding HBE:

$$\frac{\mathrm{d}}{\mathrm{d}t}\boldsymbol{F}_a = \boldsymbol{F}_a \times \gamma_a \boldsymbol{B} + \left(-\frac{7}{16}\Gamma_{\rm SDT} + \frac{5}{16}\Gamma_{\rm SE}\right)\boldsymbol{F}_a + \left(\frac{15}{16}\Gamma_{\rm SDT} - \frac{5}{16}\Gamma_{\rm SE}\right)\boldsymbol{F}_b + \frac{5}{8}R_{\rm op}\boldsymbol{s}, \tag{12}$$

$$\frac{\mathrm{d}}{\mathrm{d}t}\boldsymbol{F}_b = \boldsymbol{F}_b \times \gamma_b \boldsymbol{B} + \left(\frac{3}{16}\Gamma_{\rm SDT} - \frac{1}{16}\Gamma_{\rm SE}\right)\boldsymbol{F}_a + \left(-\frac{11}{16}\Gamma_{\rm SDT} + \frac{1}{16}\Gamma_{\rm SE}\right)\boldsymbol{F}_b - \frac{1}{8}R_{\rm op}\boldsymbol{s}. \tag{13}$$

3. Relaxation in the dark

Extensive studies have investigated the relaxation dynamics of alkali-metal ensembles, particularly under the influence of spin-exchange collisions. The seminal work by Happer[17] provided a comprehensive theoretical explanation for the narrowing of magnetic resonance linewidths at high SE rates and low magnetic fields, laying the foundation for the concept of relaxation suppression in the SERF regime. The nonlinear component of the SE interaction was later shown by Katz *et al.*[18] to eliminate the relaxation of higher-order spin moments. In a subsequent study, they also demonstrated cross-relaxation effects arising from inter-species SE collisions, particularly between a dominant species (rubidium) and a minor species (potassium). More recently, Xiao[13] employed the HBE to reproduce Happer's results and further explored AC-field-induced relaxation mechanisms. In this section, we investigate both of the transverse and longitudinal relaxations of spin polarization when SD and SE collisions are present simultaneously.

3.1. Transverse relaxation

The evolution of the transverse spin polarizations

$$F_{a+} = F_{ax} + \mathrm{i}F_{ay}, \tag{14}$$

$$F_{b+} = F_{bx} + \mathrm{i}F_{by}, \tag{15}$$

in a static magnetic field $\boldsymbol{B} = B\hat{z}$ is given by

$$\frac{\mathrm{d}}{\mathrm{d}t}\begin{pmatrix} F_{a+} \\ F_{b+} \end{pmatrix} = \boldsymbol{G}_+ \begin{pmatrix} F_{a+} \\ F_{b+} \end{pmatrix}, \tag{16}$$

where the transverse evolution matrix $\boldsymbol{G}_+$ is

$$\boldsymbol{G}_+ = \begin{pmatrix} -\mathrm{i}\omega_0 - \frac{7}{16}\Gamma_{\rm SD} - \frac{1}{8}\Gamma_{\rm SE} & \frac{15}{16}\Gamma_{\rm SD} + \frac{5}{8}\Gamma_{\rm SE} \\ \frac{3}{16}\Gamma_{\rm SD} + \frac{1}{8}\Gamma_{\rm SE} & \mathrm{i}\omega_0 - \frac{11}{16}\Gamma_{\rm SD} - \frac{5}{8}\Gamma_{\rm SE} \end{pmatrix}. \tag{17}$$

Here, $\omega_0 = \gamma B$ is the Larmor frequency, with the gyromagnetic ratio defined as $\gamma = \gamma_a = -\gamma_b$ for the two hyperfine manifolds. The real part of the eigenvalues of $\boldsymbol{G}_+$ gives the relaxation rates and the imaginary part gives the effective Larmor frequency of the transverse spin. The two eigenvalues of $\boldsymbol{G}_+$ are

$$\lambda_\pm = \frac{1}{16}\left[-9\Gamma_{\rm SD} - 6\Gamma_{\rm SE} \pm \sqrt{36\Gamma_{\rm SE}^2 - 128\mathrm{i}\omega_0\Gamma_{\rm SE} - 256\omega_0^2 + 49\Gamma_{\rm SD}^2 - 64\mathrm{i}\Gamma_{\rm SD}\omega_0 + 76\Gamma_{\rm SD}\Gamma_{\rm SE}}\right]. \tag{18}$$

Compared to Happer's original treatment,[17] Eq. (18) includes both SE and SD interactions, while neglecting wall relaxation, which is usually treated as a complete depolarization process.[14] Figure 1 presents a detailed analysis of the slow-decay

relaxation mode under various collisional regimes. As discussed in earlier theoretical works,[12,16,17] the slowest-decaying eigenmode of the transverse evolution matrix dominantly determines the system's relaxation behavior in magnetometry experiments.

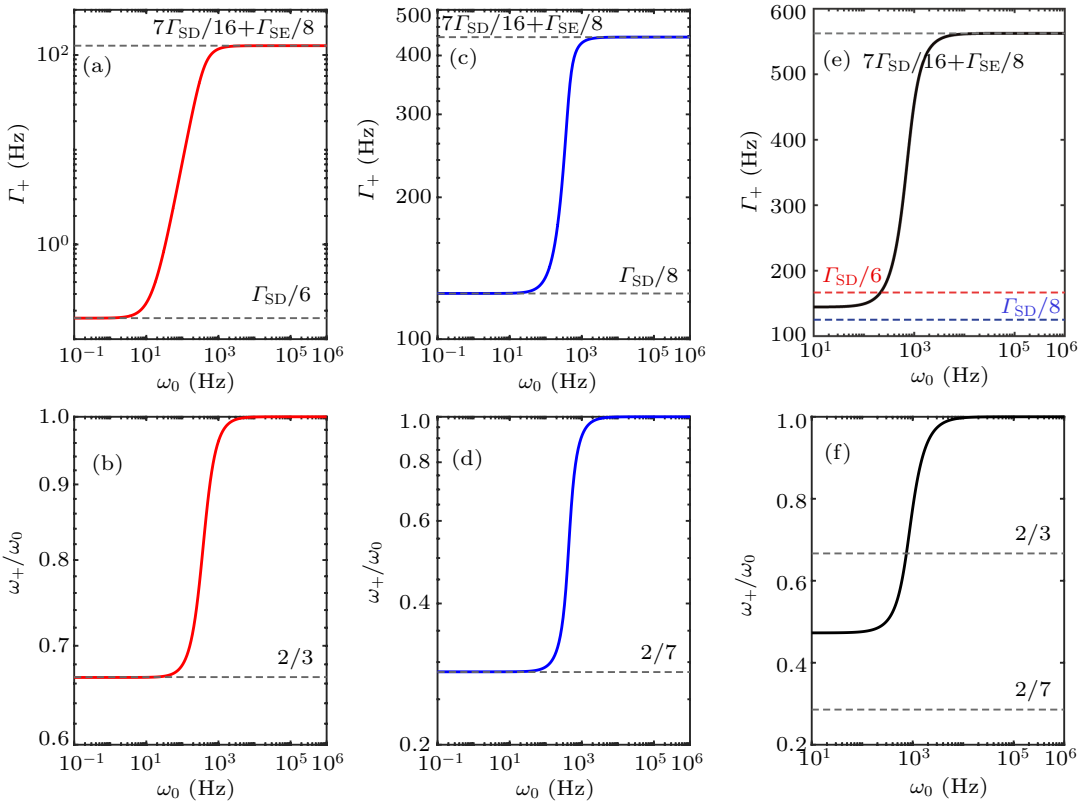


Fig. 1. Relaxation rates and effective Larmor frequency of the slow-decay mode under different collisional regimes. (a)–(b) Spin-exchange-collisions dominant regime: $\Gamma_{SE} = 2\pi \times 1000$ Hz and $\Gamma_{SD} = 2\pi \times 1$ Hz. (c)–(d) Spin-destruction-collisions dominant regime: $\Gamma_{SE} = 2\pi \times 1$ Hz and $\Gamma_{SD} = 2\pi \times 1000$ Hz. (e)–(f) Comparable SE and SD rates: $\Gamma_{SE} = \Gamma_{SD} = 2\pi \times 1000$ Hz. The parameter values shown here are chosen as theoretical examples to illustrate the characteristic behaviors in different collisional regimes and are not intended to correspond to specific experimental parameter sets.

Figures 1(a), 1(c), and 1(e) show the relaxation rates $\Gamma_+ = -\mathrm{Re}[\lambda_+]$ of the slow mode as a function of the Larmor frequency ω_0, under three representative cases: SE-dominant, SD-dominant, and comparable SD and SE rates. In the low-field limit, where $\omega_0 \ll \Gamma_{SE}, \Gamma_{SD}$, both SD and SE collisions suppress relaxation. Specifically, in the SE-dominant regime [Fig. 1(a)], the relaxation rate approaches a minimum value of $\Gamma_{SD}/6$, consistent with the SERF theory. Conversely, in the SD-dominant case [Fig. 1(c)], the low-field limit yields $\Gamma_{SD}/8$. In the high-field regime ($\omega_0 \gg \Gamma_{SE}, \Gamma_{SD}$), the relaxation rate saturates at

$$\Gamma_+ = \frac{7}{16}\Gamma_{SD} + \frac{1}{8}\Gamma_{SE}, \tag{19}$$

in agreement with our previous result reported in Ref. [16].

In the intermediate case where $\Gamma_{SE} \approx \Gamma_{SD}$ [Fig. 1(e)], the relaxation suppression in the low-field regime reflects the combined effect of both mechanisms, while the high-field saturation remains unchanged.

Figures 1(b), 1(d), and 1(f) display the corresponding effective Larmor frequencies $\omega_+ = \mathrm{Im}[\lambda_+]$, illustrating that in the low-field limit, both SD and SE collisions contribute to the suppression of spin precession. The reduction of the effective Larmor frequency reflects a combined effect of these two interactions. At higher fields, ω_+ gradually approaches the unperturbed Larmor frequency ω_0, indicating that the transverse spin dynamics become increasingly governed by the intrinsic precession of the a and b components, with reduced coupling induced by collisions.

3.2. Longitudinal relaxation

The time evolution of the longitudinal spin polarization F_{az} and F_{bz} is governed by the following differential equation:

$$\frac{\mathrm{d}}{\mathrm{d}t}\begin{pmatrix} F_{az} \\ F_{bz} \end{pmatrix} = \boldsymbol{G}_z \begin{pmatrix} F_{az} \\ F_{bz} \end{pmatrix}, \tag{20}$$

where the longitudinal evolution matrix $\boldsymbol{G}_z$ is given by

$$\boldsymbol{G}_z = \begin{pmatrix} -\frac{7}{16}\Gamma_{SD} - \frac{1}{8}\Gamma_{SE} & \frac{15}{16}\Gamma_{SD} + \frac{5}{8}\Gamma_{SE} \\ \frac{3}{16}\Gamma_{SD} + \frac{1}{8}\Gamma_{SE} & -\frac{11}{16}\Gamma_{SD} - \frac{5}{8}\Gamma_{SE} \end{pmatrix}. \tag{21}$$

The longitudinal evolution matrix $\boldsymbol{G}_z$ differs from the transverse evolution matrix $\boldsymbol{G}_+$ by a diagonal matrix

$$\boldsymbol{G}_B = \mathrm{diag}(-\mathrm{i}\omega_0, \mathrm{i}\omega_0), \tag{22}$$

which induces Larmor precession of $\boldsymbol{F}_a$ and $\boldsymbol{F}_b$ around the magnetic field $\boldsymbol{B}$ with opposite directions. The longitudinal

decay of the spin polarization can be determined by just setting $\omega_0 = 0$ in Eq. (18):

$$\frac{\lambda_\pm}{\Gamma_{\rm SD}} = \frac{1}{16}\left(-9-6\eta \pm \sqrt{49+76\eta+36\eta^2}\right), \tag{23}$$

where we have defined the relative spin-exchange strength $\eta = \Gamma_{\rm SE}/\Gamma_{\rm SD}$.

Figure 2 illustrates the dependence of the longitudinal relaxation rates on the relative spin-exchange strength. The slow-mode relaxation rate $\Gamma_+ = -{\rm Re}[\lambda_+]$, shown as the lower branch, increases gradually with increasing η, ranging from $\Gamma_{\rm SD}/8$ in the SD-dominated limit to $\Gamma_{\rm SD}/6$ in the SE-dominated limit.

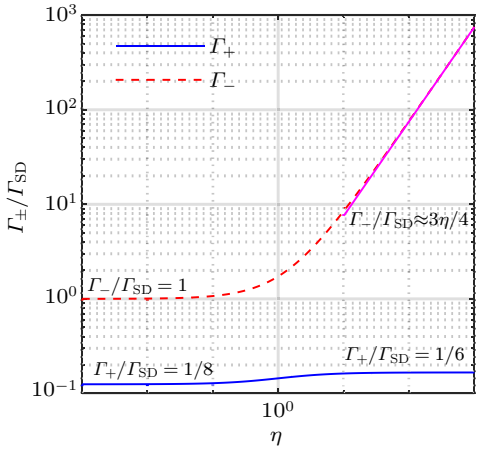


Fig. 2. Variation of the longitudinal relaxation rates $\Gamma_\pm = -{\rm Re}[\lambda_\pm]$ with respect to the relative SE strength $\eta = \Gamma_{\rm SE}/\Gamma_{\rm SD}$. The magenta solid line denotes the asymptotic behavior of the fast-decay-mode relaxation rate as $\eta \gg 1$.

Notably, these two limiting values correspond exactly to the low-field limits of the transverse relaxation rates obtained in Fig. 1. Specifically, $\Gamma_{\rm SD}/8$ matches the transverse relaxation rate in the regime $\omega_0 \ll \Gamma_{\rm SD}$, while $\Gamma_{\rm SD}/6$ corresponds to the result in the regime $\omega_0 \ll \Gamma_{\rm SE}$. This agreement is physically intuitive: as the magnetic field tends to zero, the system becomes spatially isotropic, and there is no distinction between longitudinal and transverse directions. As a result, the relaxation dynamics of all spin components converge, and the longitudinal and transverse relaxation rates coincide.

4. Effects of SE and SD collisions on the magnetometer signal response

While the longitudinal and transverse relaxation rates of alkali-metal spin polarization are widely used as theoretical indicators of magnetometric sensitivity,[7,8,10] they do not fully capture the experimentally observed signal behavior. These rates are useful for understanding how spin coherence decays under various relaxation mechanisms, but they do not directly represent the signal measured in a working magnetometer.

In practical atomic magnetometry, the measured signal is typically derived from the optical rotation of a probe beam (Faraday rotation), which reflects the steady-state spin polarization — either a specific spin component or the transverse polarization amplitude. To provide a more complete and experimentally relevant characterization, we analyze how the magnetometer signal — its amplitude, linewidth, and peak position — depends on the spin-destruction and spin-exchange collision rates.

In the following, we examine how these two types of collisions influence both the sensitivity and accuracy of field detection, using two representative magnetometer configurations: the conventional SERF setup and the magnetic-resonance Mx-type magnetometer. This analysis extends the previous discussion of relaxation rates and bridges the gap between microscopic spin dynamics and macroscopic signal response.

4.1. The zero-resonance magnetometer

In the classic SERF magnetometer configuration,[7,10] two laser beams are employed to polarize and probe the atomic vapor. A circularly polarized pump beam propagating along the z-axis is used to optically polarize the alkali-metal atoms, aligning their spin orientation along the pump direction. A linearly polarized probe beam, directed along the y-axis, then monitors the spin dynamics via Faraday rotation. The probe's polarization rotation angle provides a direct measure of the transverse spin component $\langle S_y \rangle$, which serves as the magnetometric signal.

In this geometry, the system is most sensitive to magnetic fields B_x along the x-axis, as such fields induce spin precession with the largest projection onto the y-axis — precisely the direction probed by the Faraday rotation signal.

The steady electronic spin polarization $\boldsymbol{S}^{(\rm s)}$ can be readily obtained by deriving the steady solution of Eqs. (4) and (5):

$$S_x^{(\rm s)} = 0, \tag{24}$$

$$S_y^{(\rm s)} = S_0 \frac{(1+2I)\beta_x}{1+(1+2I)^2\beta_x^2}, \tag{25}$$

$$S_z^{(\rm s)} = S_0 \frac{1}{1+(1+2I)^2\beta_x^2}, \tag{26}$$

where

$$S_0 = \frac{R_{\rm op}}{2(\Gamma_{\rm SD}+R_{\rm op})} \tag{27}$$

is the steady polarization under the action of pumping and relaxation, and

$$\beta_x = \frac{\gamma B_x}{R_{\rm op}+\Gamma_{\rm SD}} \tag{28}$$

is the normalized Larmor frequency. It is evident from Eqs. (25) and (26) that the steady-state spin components $S_y^{(\rm s)}$ and $S_z^{(\rm s)}$ are determined by the optical pumping rate $R_{\rm op}$, the spin-destruction rate $\Gamma_{\rm SD}$, and the nuclear spin I. Although spin-exchange collisions play an important role in driving the spin system toward equilibrium, they do not affect the final steady-state polarization values.

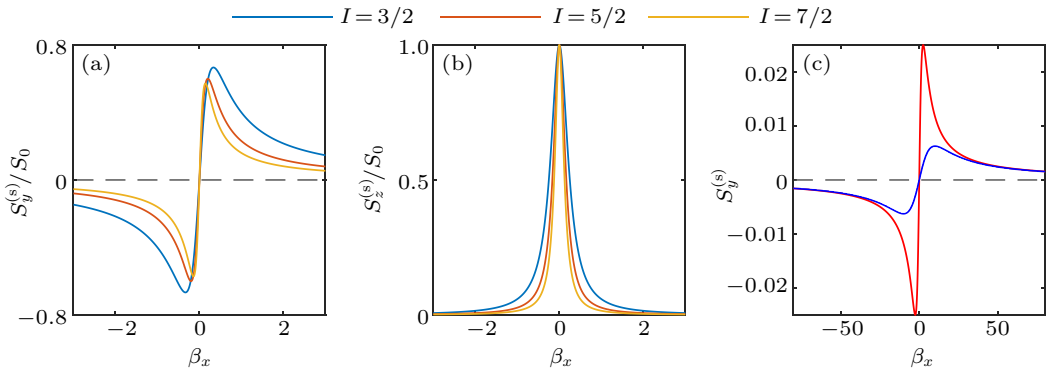


Fig. 3. Steady-state polarization as a function of the normalized Larmor frequency β_x. (a)–(b) Dependence of $S_y^{(s)}$ and $S_z^{(s)}$ on β_x for different nuclear spins I. (c) Dependence of $S_y^{(s)}$ on β_x for different spin-destruction rates $\Gamma_{SD} = 9R_{op}$ (red) and $\Gamma_{SD} = 39R_{op}$ (blue), with nuclear spin fixed at $I = 3/2$. These correspond to total relaxation rates $\Gamma_0 = 10R_{op}$ and $\Gamma_0 = 40R_{op}$, respectively.

The linewidth, defined as the full width at half maximum (FWHM) of the resonant signal $S_z^{(s)}$ or the dispersive signal $S_y^{(s)}$, is determined by the spin-destruction rate Γ_{SD}, the optical pumping rate R_{op}, and the nuclear spin I. Figures 3(a) and 3(b) illustrate the dependence of the steady-state spin components $S_y^{(s)}$ and $S_z^{(s)}$ on the normalized Larmor frequency β_x (or equivalently the magnetic field B_x), for different nuclear spin values $I = 3/2, 5/2, 7/2$. The curves clearly show that, for identical spin-destruction and optical pumping rates, atoms with larger nuclear spin exhibit narrower linewidths.

The dispersive signal $S_y^{(s)}$ as a function of β_x for two representative values of $\Gamma_0 = R_{op} + \Gamma_{SD}$ is shown in Fig. 3(c), assuming $I = 3/2$. It is evident that a larger Γ_0 leads to broader linewidths and reduced signal response at a given magnetic field B_x, indicating a degradation of the magnetometer sensitivity.

To enhance the sensitivity of SERF magnetometers, it is therefore essential to minimize the spin-destruction rate Γ_{SD}. In anti-relaxation-coated or high-pressure buffer-gas cells, the total spin-destruction rate $\Gamma_{SD} = \Gamma_{SD}^{self} + \Gamma_{SD}^{AX}$ arises from both alkali–alkali atomic collisions $\Gamma_{SD}^{self} = n_A \sigma_{self}^{SD} \bar{v}_{self}$ and alkali–buffer (or quenching) gas collisions $\Gamma_{SD}^{AX} = n_X \sigma_X^{SD} \bar{v}_{AX}$. Here n_A and n_X denote the number densities of alkali-metal atoms and buffer (or quenching) gas, respectively; σ_{self}^{SD} and σ_X^{SD} are the intrinsic and alkali–buffer SD cross sections, and $\bar{v}_{self}$, and $\bar{v}_{AX}$ are the mean relative velocities of the colliding particles, typically on the order of 10^2 m/s.

Table 1 summarizes the spin-destruction cross sections for several alkali-metal atoms interacting with different buffer gases. The data indicate that, for a given alkali-metal atomic density n_A and buffer-gas density n_X, the total spin-destruction rate Γ_{SD} is minimized for potassium atoms in helium among the listed combinations. This property makes the K–He system particularly favorable for achieving narrow linewidths and high sensitivity in SERF magnetometry.

Table 1. Spin-destruction cross sections of alkali-metal atoms (in cm^2). Values marked with a superscript * are theoretical estimates from Ref. [22].

Alkali metal	σ_{Self}^{SD}	σ_{He}^{SD}	σ_{Ne}^{SD}	$\sigma_{N_2}^{SD}$
K	1×10^{-18} [19]	8×10^{-25} [20,21]	1×10^{-23} [21]	7.9×10^{-23} [10]
Rb	9×10^{-18} [20]	9×10^{-24} [20]	1.8×10^{-23}* [22]	1×10^{-22} [23]
Cs	2×10^{-16} [24]	3×10^{-23} [25]	2×10^{-23}* [22]	6×10^{-22} [25]

4.2. The Mx magnetometer configuration

In this section, we consider an Mx-type atomic magnetometer, in which alkali-metal atoms are simultaneously subjected to a rotating magnetic field in the x–y plane and a static magnetic field along the $\hat{z}$ direction:

$$\boldsymbol{B}(t) = (B_1 \cos\omega t,\ B_1 \sin\omega t,\ B_0), \tag{29}$$

accompanied by longitudinal optical pumping characterized by $\boldsymbol{s} = (0,0,1)$.

To simplify the treatment of the spin dynamics under this time-dependent field, we transform to a rotating frame co-rotating with the transverse drive at frequency ω. The transverse spin components in the rotating frame are defined as

$$f_{a+} = \mathrm{e}^{-\mathrm{i}\omega t} F_{a+}, \tag{30}$$

$$f_{b+} = \mathrm{e}^{-\mathrm{i}\omega t} F_{b+}, \tag{31}$$

where $f_{a+} = f_{ax} + \mathrm{i} f_{ay}$ and $f_{b+} = f_{bx} + \mathrm{i} f_{by}$ denote the complex transverse spin polarizations for the a and b manifolds, respectively.

In this rotating frame, the spin dynamics are governed by a linear system

$$\frac{\mathrm{d}}{\mathrm{d}t}\boldsymbol{f} = (\boldsymbol{G}_0 + \boldsymbol{G}_{drv})\boldsymbol{f} + \boldsymbol{v}_{op}, \tag{32}$$

where $\boldsymbol{f} = (f_{ax}, f_{ay}, f_{bx}, f_{by}, f_{az}, f_{bz})^{\mathrm{T}}$ collects the rotating-frame spin components.

The matrix $\boldsymbol{G}_0$ encapsulates the effects of spin precession and relaxation and can be expressed as a direct sum of a 4×4 transverse block and a 2×2 longitudinal block:

$$\boldsymbol{G}_0 = \begin{bmatrix} -\frac{7\Gamma_0}{16}-\frac{\Gamma_{\rm SE}}{8} & \omega+\omega_0 & \frac{15\Gamma_0}{16}+\frac{5\Gamma_{\rm SE}}{8} & 0 \\ -\omega-\omega_0 & -\frac{7\Gamma_0}{16}-\frac{\Gamma_{\rm SE}}{8} & 0 & \frac{15\Gamma_0}{16}+\frac{5\Gamma_{\rm SE}}{8} \\ \frac{3\Gamma_0}{16}+\frac{\Gamma_{\rm SE}}{8} & 0 & -\frac{11\Gamma_0}{16}-\frac{5\Gamma_{\rm SE}}{8} & \omega-\omega_0 \\ 0 & \frac{3\Gamma_0}{16}+\frac{\Gamma_{\rm SE}}{8} & -\omega+\omega_0 & -\frac{11\Gamma_0}{16}-\frac{5\Gamma_{\rm SE}}{8} \end{bmatrix} \oplus \begin{bmatrix} -\frac{7\Gamma_0}{16}-\frac{\Gamma_{\rm SE}}{8} & \frac{15\Gamma_0}{16}+\frac{5\Gamma_{\rm SE}}{8} \\ \frac{3\Gamma_0}{16}+\frac{\Gamma_{\rm SE}}{8} & -\frac{11\Gamma_0}{16}-\frac{5\Gamma_{\rm SE}}{8} \end{bmatrix}. \tag{33}$$

The drive matrix

$$\boldsymbol{G}_{\rm drv} = \omega_1 \begin{pmatrix} 0 & 0 & 0 & 0 & 0 & 0 \\ 0 & 0 & 0 & 0 & 1 & 0 \\ 0 & 0 & 0 & 0 & 0 & 0 \\ 0 & 0 & 0 & 0 & 0 & 1 \\ 0 & -1 & 0 & 0 & 0 & 0 \\ 0 & 0 & 0 & -1 & 0 & 0 \end{pmatrix} \tag{34}$$

describes the coupling induced by the rotating transverse field, with $\omega_1 = \gamma B_1$ representing the driving strength.

The source term from optical pumping is given by

$$\boldsymbol{v}_{\rm op} = R_{\rm op} \left(0\ 0\ 0\ 0\ \tfrac{5}{8}\ -\tfrac{1}{8}\right)^{\rm T}. \tag{35}$$

The steady-state spin polarization is then obtained by solving

$$\boldsymbol{f}^{(\rm s)} = -(\boldsymbol{G}_0 + \boldsymbol{G}_{\rm drv})^{-1} \boldsymbol{v}_{\rm op}. \tag{36}$$

Since the probe beam measures transverse spin components in the laboratory frame, we transform back using Eqs. (30) and (31):

$$F_x^{(\rm s)} = \cos(\omega t)\left[f_{ax}^{(\rm s)} + f_{bx}^{(\rm s)}\right] - \sin(\omega t)\left[f_{ay}^{(\rm s)} + f_{by}^{(\rm s)}\right], \tag{37}$$

$$F_y^{(\rm s)} = \sin(\omega t)\left[f_{ax}^{(\rm s)} + f_{bx}^{(\rm s)}\right] + \cos(\omega t)\left[f_{ay}^{(\rm s)} + f_{by}^{(\rm s)}\right]. \tag{38}$$

The detected electronic spin signal (e.g., via Faraday rotation of a linearly polarized, far-off-resonant probe beam) is proportional to the transverse electron spin polarization:[5,7,10]

$$S_x^{(\rm s)} = \frac{1}{2I+1}\Big[(f_{ax}^{(\rm s)} - f_{bx}^{(\rm s)})\cos(\omega t) - (f_{ay}^{(\rm s)} - f_{by}^{(\rm s)})\sin(\omega t)\Big], \tag{39}$$

$$S_y^{(\rm s)} = \frac{1}{2I+1}\Big[(f_{ax}^{(\rm s)} - f_{bx}^{(\rm s)})\sin(\omega t) + (f_{ay}^{(\rm s)} - f_{by}^{(\rm s)})\cos(\omega t)\Big]. \tag{40}$$

When demodulated using a lock-in amplifier with quadrature reference signals,[26] the signal amplitude corresponds to

$$A_\perp = \frac{1}{2I+1}\sqrt{\left(f_{ax}^{(\rm s)} - f_{bx}^{(\rm s)}\right)^2 + \left(f_{ay}^{(\rm s)} - f_{by}^{(\rm s)}\right)^2}, \tag{41}$$

which serves as the primary output of the Mx-type magnetometer.

Figure 4 shows the frequency response of the amplitude function $A_\perp$ under different values of the static magnetic field B_0. As the magnetic field increases from panel (a) to (c), the resonance structure transforms from a single peak to two well-separated peaks. At very low magnetic field ($B_0 = 1$ nT), shown in Fig. 4(a), the resonance linewidth — set by the combined spin-exchange, spin-destruction, and optical pumping rates — is significantly larger than the Larmor frequency. As a result, the resonances associated with the a- and b-manifolds overlap, producing a single broadened peak. When the static field is increased to $B_0 = 1000$ nT [Fig. 4(b)], the Larmor frequency becomes comparable to the linewidth, and the individual contributions begin to resolve. This results in a visible shoulder in the spectrum, attributed to the emerging b-manifold resonance. At even higher field ($B_0 = 10000$ nT) [Fig. 4(c)], where the Larmor frequency $|\gamma B_0|$ is much larger than the resonance linewidth, the two resonances become fully separated, clearly distinguishing the a- and b-manifold responses.

While Fig. 4 illustrates the overall resonance profile of the Mx-type magnetometer signal, a more quantitative characterization of its performance requires analyzing two key spectral features: the resonance linewidth and the peak frequency position. The linewidth, defined as the full width at half maximum of the amplitude response function $A_\perp$, serves

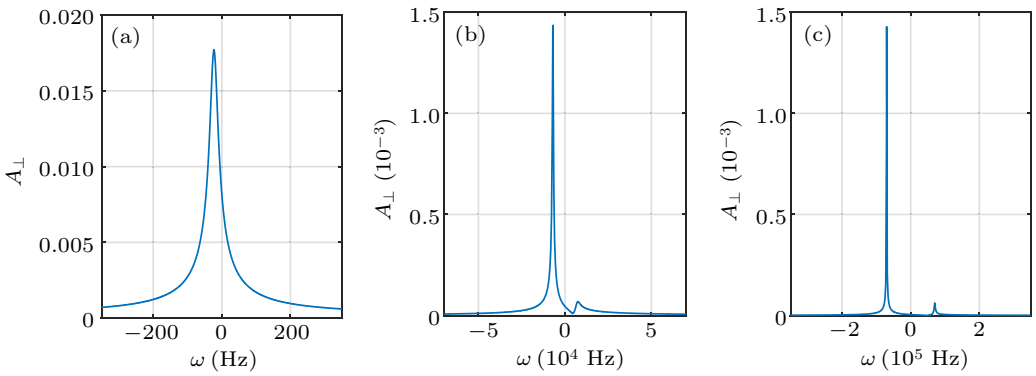


Fig. 4. Typical behavior of the steady-state transverse spin signal amplitude $A_\perp$ as a function of the RF driving frequency ω, shown for different values of the static magnetic field B_0: (a) $B_0 = 1$ nT, (b) $B_0 = 1000$ nT, (c) $B_0 = 10000$ nT. The spin-exchange rate is fixed at $\Gamma_{\rm SE} = 2\pi \times 2000$ Hz, the spin-destruction rate at $\Gamma_{\rm SD} = 2\pi \times 50$ Hz, and the optical pumping rate is set to $R_{\rm op} = 0.1\Gamma_{\rm SD}$ for all panels. The gyromagnetic ratio is taken to be $\gamma = 2\pi \times 7$ Hz/nT. The sign of the the driving frequency ω corresponds to the handedness of the rotating magnetic field.

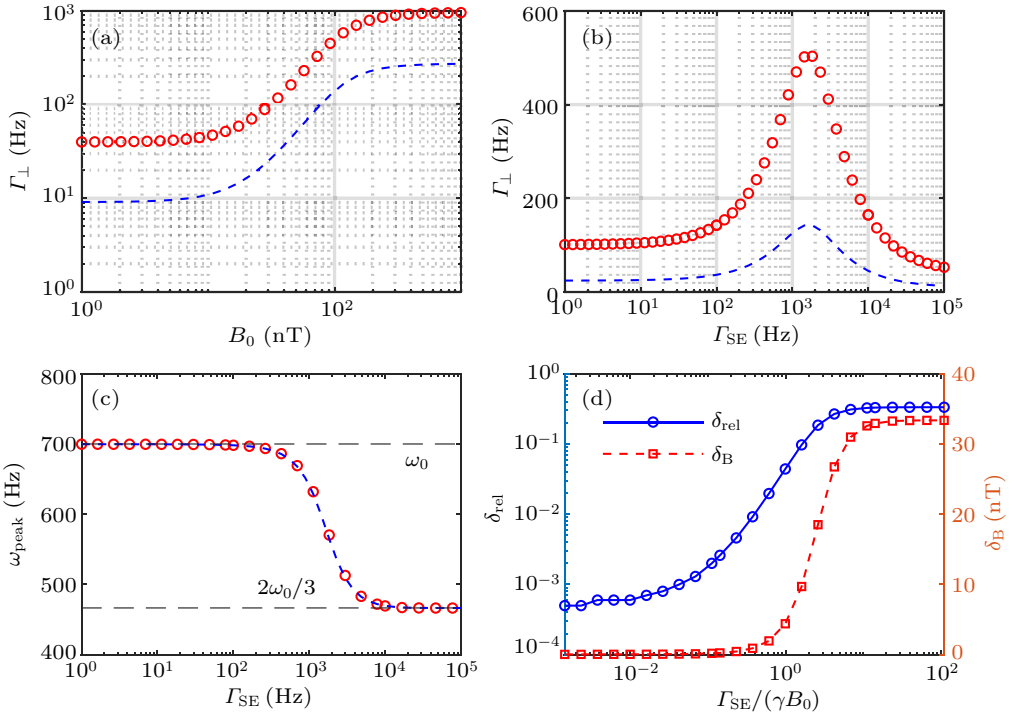


Fig. 5. (a) Resonance linewidth $\Gamma_\perp$ as a function of the static magnetic field B_0, with fixed parameters: $\Gamma_{\rm SE} = 2\pi \times 2000$ Hz, $\Gamma_{\rm SD} = 2\pi \times 50$ Hz, $R_{\rm op} = 0.1\,\Gamma_{\rm SD}$, $B_1 = 1$ nT, and $\gamma = 2\pi \times 7$ Hz/nT. (b), (c) Dependence of the resonance linewidth $\Gamma_\perp$ and the peak response frequency $\omega_{\rm peak}$ on the spin-exchange rate $\Gamma_{\rm SE}$, with the static field fixed at $B_0 = 100$ nT. All other parameters are identical to those in panel (a). (d) Relative error $\delta_{\rm rel}$ and absolute field error $\delta_{\rm B}$ as functions of the normalized spin-exchange rate $\Gamma_{\rm SE}/(\gamma B_0)$. Parameters are the same as in panel (c). In panels (a)–(c), the dashed blue lines correspond to the theoretical decay rate and precession frequency of the slow-decay mode, as given by Eq. (18).

as a direct indicator of the magnetometer's sensitivit — narrower linewidths generally enable more precise detection of small magnetic field variations. On the other hand, the deviation of the peak response frequency from the actual Larmor frequency reflects the measurement accuracy, especially under strong spin-exchange collisions.

Figure 5 presents a quantitative characterization of the amplitude response function $A_\perp$ under varying static field strengths B_0 and spin-exchange rates $\Gamma_{\rm SE}$. Figures 5(a) and 5(b) demonstrate that the linewidth $\Gamma_\perp$ exhibits a clear SERF-like suppression behavior as B_0 decreases or relatively $\Gamma_{\rm SE}$ increases, qualitatively consistent with the analytic expression for the slow-decay transverse relaxation rate Γ_+ given by Eq. (18). However, the simulation results clearly show that the actual linewidths extracted from $A_\perp$ are significantly broader than those predicted by Γ_+ alone.

This discrepancy highlights an important physical insight: the linewidth of the measured signal is governed not solely by the intrinsic spin relaxation rate, but also depends on how the observable is constructed. In this case, the measured signal corresponds to the steady-state amplitude of the transverse spin polarization, which is determined by the steady-state solution of the spin dynamics under simultaneous pumping and transverse RF excitation. Consequently, power broadening effects and the nonlinear response of $A_\perp$ to the driving field contribute to an effective broadening beyond that captured by Γ_+.

Moreover, Fig. 5(c) shows that the peak frequency $\omega_{\rm peak}$ increasingly deviates from the nominal Larmor frequency ω_0 as the spin-exchange rate $\Gamma_{\rm SE}$ rises. This deviation reflects the measurement inaccuracy introduced by spin-exchange interactions and serves as a quantitative proxy for evaluating magnetometer performance.

To more clearly demonstrate how $\Gamma_{\rm SE}$ influences field measurement accuracy, Fig. 5(d) presents both the relative error, defined as $\delta_{\rm rel} = (\gamma B_0 - \omega_{\rm peak})/(\gamma B_0)$, and the absolute field error, given by $\delta_{\rm B} = (\gamma B_0 - \omega_{\rm peak})/\gamma$, as functions of the dimensionless parameter $\Gamma_{\rm SE}/(\gamma B_0)$.

These results reveal a clear trend: in the strong SERF regime ($\Gamma_{\rm SE}/\gamma B_0 \gg 1$), the peak frequency significantly departs from the true Larmor value, leading to poor reconstruction accuracy. Conversely, in the opposite limit $\Gamma_{\rm SE}/\gamma B_0 \ll 1$ — corresponding to either reduced spin-exchange or enhanced magnetic fields — the deviations are markedly suppressed. In this regime, the relative error drops to $\delta_{\rm rel} \sim 10^{-4}$ and the absolute field error $\delta_{\rm B}$ is reduced below 1 nT, indicating excellent field measurement fidelity.

5. Conclusion

We have investigated the role of spin-destruction and spin-exchange collisions in determining spin relaxation and magnetometric response in alkali-metal vapors, based on a hyperfine-resolved Bloch equation. Our analysis shows that both SD and SE collisions contribute to the suppression of transverse relaxation and spin precession in the low-field regime, while longitudinal relaxation is largely governed by

SD interactions and exhibits weak dependence on the SE rate.

Applying this framework, we explored how these collisional processes influence the performance of SERF and Mx-type magnetometers. The SERF magnetometer's response is primarily determined by the SD rate and shows limited sensitivity to the nuclear spin quantum number. In contrast, the Mx-type magnetometer's sensitivity and accuracy are strongly affected by both magnetic field strength and the SE rate. In particular, accurate magnetic field reconstruction with Mx-type magnetometers requires operating in the high-field regime, where the Larmor frequency significantly exceeds the spin-exchange rate — even though this comes at the cost of reduced sensitivity. These findings provide practical insights for optimizing magnetometer design and operation under varying experimental conditions.

Appendix A: Derivation of the hyperfine Bloch equation

The density matrix ρ can be expanded in different operator bases, such as the coupled basis $|F,m_F\rangle\langle F',m_{F'}|$ or the spherical tensor operator basis.[6,17] In this work, we adopt the latter, defined as

$$T_{\mathrm{LM}}(FF') = \sum_m (-1)^{m-M-F'} \times C^{L,M}_{F,m;F',M-m} |F,m\rangle\langle F',m-M|, \tag{A1}$$

where C denotes the Clebsch–Gordan coefficients. This basis is particularly convenient for deriving the evolution equations of the total angular momentum components $\boldsymbol{F}_{a,b}$, since the vector operators $\boldsymbol{F}_a$ and $\boldsymbol{F}_b$ correspond to rank-1 spherical tensors:[27]

$$F_{a,M} = \sqrt{\frac{a(a+1)(2a+1)}{3}}\, T_{1M}(aa), \tag{A2}$$

$$F_{b,M} = \sqrt{\frac{b(b+1)(2b+1)}{3}}\, T_{1M}(bb), \tag{A3}$$

where $F_{a,M}$ and $F_{b,M}$ denote the spherical components of $\boldsymbol{F}_a$ and $\boldsymbol{F}_b$, respectively. Therefore, to obtain the time evolution of the spin expectation values $\langle \boldsymbol{F}_a\rangle$ and $\langle \boldsymbol{F}_b\rangle$, it suffices to derive the dynamical equations for the corresponding tensor components $\langle T_{1M}(aa)\rangle$ and $\langle T_{1M}(bb)\rangle$.

To derive the evolution equation for $\langle T_{\mathrm{LM}}(FF)\rangle$, we rewrite the master equation (1) as

$$\frac{\mathrm{d}\rho}{\mathrm{d}t} = \underbrace{\frac{A_{\mathrm{hf}}}{\mathrm{i}\hbar}[\boldsymbol{I}\cdot\boldsymbol{S},\rho]}_{\mathrm{hf}} + \underbrace{\frac{g_s\mu_{\mathrm{B}}}{\mathrm{i}\hbar}[\boldsymbol{B}\cdot\boldsymbol{S},\rho]}_{\mathrm{Zeeman}} + \underbrace{\Gamma_{\mathrm{SDT}}(\varphi-\rho)}_{\text{S-Damping}} + \underbrace{4\Gamma_{\mathrm{SE}}\varphi\langle\boldsymbol{S}\rangle\cdot\boldsymbol{S}}_{\mathrm{SE}} + \underbrace{2R_{\mathrm{op}}\varphi\, \boldsymbol{s}\cdot\boldsymbol{S}}_{\mathrm{OP}}, \tag{A4}$$

and evaluate the contribution of each term to the dynamics of $\langle T_{\mathrm{LM}}(FF)\rangle$.

The hyperfine interaction does not contribute to the evolution of $\langle T_{\mathrm{LM}}(FF)\rangle$,

$$\left[\frac{\mathrm{d}}{\mathrm{d}t}\langle T_{\mathrm{LM}}(FF)\rangle\right]_{\mathrm{hf}} = \mathrm{Tr}\left[T_{\mathrm{LM}}(FF)\frac{A_{\mathrm{hf}}}{\mathrm{i}\hbar}[\boldsymbol{I}\cdot\boldsymbol{S},\rho]\right] = 0; \tag{A5}$$

and the Zeeman interaction leads to Larmor precession of the angular momentum

$$\frac{\mathrm{d}}{\mathrm{d}t}\langle \boldsymbol{F}_a\rangle = \gamma_a\langle \boldsymbol{F}_a\rangle\times\boldsymbol{B}, \tag{A6}$$

$$\frac{\mathrm{d}}{\mathrm{d}t}\langle \boldsymbol{F}_b\rangle = \gamma_b\langle \boldsymbol{F}_b\rangle\times\boldsymbol{B}. \tag{A7}$$

The S-damping term causes the evolution of $\langle T_{\mathrm{LM}}(aa)\rangle$ and $\langle T_{\mathrm{LM}}(bb)\rangle$ as follows:

$$\begin{aligned}&\frac{1}{\Gamma_{\mathrm{SDT}}}\left[\frac{\mathrm{d}}{\mathrm{d}t}\langle T_{\mathrm{LM}}(FF)\rangle\right]_{\text{S-Damping}}\\ &= -\langle T_{\mathrm{LM}}(FF)\rangle + \big[X_L(aa)\langle T_{\mathrm{LM}}(aa)\rangle\\ &\quad + X_L(bb)\langle T_{\mathrm{LM}}(bb)\rangle\big]X_L(FF),\end{aligned} \tag{A8}$$

where the coupling coefficients are given by[17]

$$X_L(FF') = \left(\frac{[F][F']}{[S]}\right)^{1/2} W(F',S,L,I;I,F), \tag{A9}$$

$$Y_L(FF') = \left(\frac{[F][F']}{[I]}\right)^{1/2} W(I,F,S,L;S,F'), \tag{A10}$$

with $[J]=2J+1$. In this treatment, we neglect contributions from hyperfine coherences such as $\langle T_{\mathrm{LM}}(F_1F_2)\rangle$ with $F_1\neq F_2$.

The contribution of the nonlinear SE term in Eq. (A4) to the evolution of $\langle T^\dagger_{\mathrm{LM}}(FF)\rangle$ is given by

$$\begin{aligned}&\frac{1}{\Gamma_{\mathrm{SE}}}\left[\frac{\mathrm{d}}{\mathrm{d}t}\langle T^\dagger_{\mathrm{LM}}(FF)\rangle\right]_{\mathrm{SE}}\\ &= \mathrm{Tr}\left[(4\varphi\langle\boldsymbol{S}\rangle\cdot\boldsymbol{S})T^\dagger_{\mathrm{LM}}(FF)\right]\\ &= [6[L]]^{\frac{1}{2}}[F]\sum_{\substack{\Lambda\mu\\F_1F_2\\F_3F_4}} X_\Lambda(F_1F_2)\langle T^+_{\Lambda\mu}(F_1F_2)\rangle Y_1(F_3F_4)\\ &\quad\times\langle T^+_{1,M-\mu}(F_3F_4)\rangle\sqrt{[\Lambda]}C^{LM}_{\Lambda\mu;1,M-\mu}\begin{pmatrix} I & S & F\\ I & S & F\\ \Lambda & 1 & L\end{pmatrix},\end{aligned} \tag{A11}$$

where the last factor denotes the Wigner $9j$ symbol.[27] Neglecting the hyperfine coherence terms (i.e., retaining only contributions with $F_1=F_2$ and $F_3=F_4$), Eq. (A11) simplifies to

$$\begin{aligned}&\frac{1}{\Gamma_{\mathrm{SE}}}\left[\frac{\mathrm{d}}{\mathrm{d}t}\langle T^\dagger_{\mathrm{LM}}(FF)\rangle\right]_{\mathrm{SE}}\\ &= \delta_{1L}Y_1(FF)\sum_{F_3}Y_1(F_3F_3)\langle T^\dagger_{1,M}(F_3F_3)\rangle\\ &\quad + [6[I]]^{1/2}[F]\sum_{\Lambda=1}^{2I}\sum_{\mu=-\Lambda}^{\Lambda}\sum_{F_1F_3}\sqrt{[\Lambda]}X_\Lambda(F_1F_1)\langle T^\dagger_{\Lambda\mu}(F_1F_1)\rangle\\ &\quad\times\langle T^\dagger_{1,M-\mu}(F_3F_3)\rangle C^{L,M}_{\Lambda,\mu;1,M-\mu}\begin{pmatrix} I & S & F\\ I & S & F\\ \Lambda & 1 & L\end{pmatrix}.\end{aligned} \tag{A12}$$

If we further neglect all nonlinear terms, we obtain the linearized form

$$\frac{1}{\Gamma_{\rm SE}}\left[\frac{\mathrm{d}}{\mathrm{d}t}\langle T^{\dagger}_{\rm LM}(FF)\right]_{\rm SE} = \delta_{1L}Y_1(FF)\sum_{F_3}Y_1(F_3F_3)\langle T^{\dagger}_{1,M}(F_3F_3)\rangle. \tag{A13}$$

This linear approximation is consistent with the treatments in Refs. [12,13,17], and is equivalent to setting $\varphi=(4I+2)^{-1}\mathcal{I}$, where $\mathcal{I}$ denotes the identity matrix in the tensor product space of the electron spin and nuclear spin. Finally, the evolution equation for $\langle T_{\rm LM}(FF)\rangle$ can be obtained using the Hermitian conjugation property of the spherical tensor operators:[28]

$$T^{\dagger}_{lm}(ff')=(-1)^{f-f'+m}T_{l,-m}(f'f). \tag{A14}$$

The contribution of the optical pumping term to the evolution of the tensor component $\langle T_{\rm LM}(FF)\rangle$ can be written as

$$\frac{1}{R_{\rm op}}\left[\frac{\mathrm{d}}{\mathrm{d}t}\langle T_{\rm LM}(FF)\rangle\right]_{\rm OP}=\delta_{1L}\frac{s_M}{\sqrt{2[I]}}Y_1(FF), \tag{A15}$$

under the same linearization approximation used in deriving Eq. (A13). Here, s_M denotes the M-th component of the photon spin vector $\boldsymbol{s}$ in the spherical basis.

By combining all the contributions — including Zeeman interaction, spin-damping, spin-exchange, and optical pumping — to the dynamics of $\langle T_{1M}(FF)\rangle$, and making use of Eqs. (A2) and (A3), we arrive at the hyperfine Bloch equations as given in Eqs. (4) and (5).

Acknowledgement

This work was supported by the Science Challenge Project (Grant No. TZ2025017).

References

[1] Zhang R, Xiao W, Ding Y D, Feng Y L, Peng X, Shen L, Sun C X, Wu T, Wu Y L, Yang Y C, Zheng Z Y, Zhang X Z, Chen J B and Guo H 2020 *Sci. Adv.* **6** eaba8792

[2] Limes M E, Foley E L, Kornack T W, Caliga S, McBride S, Braun A, Lee W, Lucivero V G and Romalis M V 2020 *Phys. Rev. Appl.* **14** 011002

[3] Jiang M, Su H W, Chen Y F, Jiao M, Huang Y, Wang Y H, Rong X, Peng X H and Du J F 2025 *Rep. Prog. Phys.* **88** 016401

[4] Wei K, Xu Z T, He Y X, Ma X L, Heng X, Huang X F, Quan W, Ji W, Liu J, Wang X P, Budker D and Fang J C 2025 *Rep. Prog. Phys.* **88** 057801

[5] Happer W, Jau Y Y and Walker T 2010 *Optically Pumped Atoms* (Weinheim: Wiley-VCH)

[6] Appelt S, Ben-Amar Baranga A, Erickson C J, Romalis M V, Young A R and Happer W 1998 *Phys. Rev. A* **58** 1412

[7] Budker D and Romalis M 2013 *Optical Magnetometry* (Cambridge: Cambridge University Press)

[8] Grosz A, Haji-Sheikh M J and Mukhopadhyay S C (eds.) 2017 *High Sensitivity Magnetometers* (Cham: Springer International Publishing)

[9] Savukov I M and Romalis M V 2005 *Phys. Rev. A* **71** 023405

[10] Seltzer S J 2008 *Developments in Alkali-Metal Atomic Magnetometry* (Ph.D. Dissertation) (Princeton University, Princeton)

[11] Bhaskar N D, Camparo J, Happer W and Sharma A 1981 *Phys. Rev. A* **23** 3048

[12] Katz O, Peleg O and Firstenberg O 2015 *Phys. Rev. Lett.* **115** 113003

[13] Xiao W, Wu T, Peng X and Guo H 2021 *Phys. Rev. A* **103** 043116

[14] Dikopoltsev M, Berrebi A, Levy U and Katz O 2025 *Phys. Rev. Lett.* **134** 143201

[15] Mouloudakis K, Vasilakis G, Lucivero V G, Kong J, Kominis I K and Mitchell M W 2022 *Phys. Rev. A* **106** 023112

[16] Tang F and Zhao N 2025 *Phys. Rev. A* **111** 013103

[17] Happer W and Tam A C 1977 *Phys. Rev. A* **16** 1877

[18] Katz O, Dikopoltsev M, Peleg O, Shuker M, Steinhauer J and Katz N 2013 *Phys. Rev. Lett.* **110** 263004

[19] Kadlecek S, Anderson L W and Walker T 1998 *Nucl. Instrum. Methods Phys. Res. A* **402** 208

[20] Ben-Amar Baranga A, Appelt S, Romalis M V, Erickson C J, Young A R, Cates G D and Happer W 1998 *Phys. Rev. Lett.* **80** 2801

[21] Franz F A and Volk C 1982 *Phys. Rev. A* **26** 85

[22] Walker T G 1989 *Phys. Rev. A* **40** 4959

[23] Wagshul M E and Chupp T E 1994 *Phys. Rev. A* **49** 3854

[24] Bhaskar N D, Pietras J, Camparo J, Happer W and Liran J 1980 *Phys. Rev. Lett.* **44** 930

[25] Beverini N, Minguzzi P and Strumia F 1971 *Phys. Rev. A* **4** 550

[26] Tang F, Li A X, Zhang K, Wang Y H and Zhao N 2019 *J. Phys. B: At. Mol. Opt. Phys.* **52** 205004

[27] Khersonskii V K, Moskalev A N and Varshalovich D A 1988 *Quantum Theory of Angular Momentum* (Singapore: World Scientific Publishing Company)

[28] Happer W 1972 *Rev. Mod. Phys.* **44** 169